

Modeling and simulation of liquid diffusion through a porous finitely elastic solid

QIANGSHENG ZHAO AND PANAYIOTIS PAPADOPOULOS*

*Department of Mechanical Engineering
University of California, Berkeley, CA 94720-1740, USA*

Table of contents

1 Introduction	2
2 Concepts, definitions and constitutive relations	4
2.1 Motion and deformation	4
2.2 Porosity, liquid volume fraction and density	4
2.3 Liquid mass flux and linear momentum	5
2.4 Effective stress	6
3 Balance laws	6
3.1 Balance of mass	7
3.2 Balance of linear momentum	8
4 Finite element implementation	8
4.1 Weak forms	8
4.2 Space and time discretization	9
5 Numerical simulations	10
5.1 Stretching of a saturated cube	10
5.2 Squeezing of a saturated cube	11
5.3 Flexure of a Nafion [®] film due to water absorption	12
6 Conclusions	13
Appendix: Consistent Linearization of the Balance Laws	14

Abstract

A new theory is proposed for the continuum modeling of liquid flow through a porous elastic solid. The solid and the voids are assumed to jointly constitute the macroscopic solid phase, while the liquid volume fraction is included as a separate state variable. A finite element implementation is employed to assess the predictive capacity of the proposed theory, with particular emphasis on the mechanical response of Nafion[®] membranes to the flow of water.

Keywords: Porous media; flow; diffusion; continuum mechanics; elasticity; finite element method; Nafion

*Corresponding author

1 Introduction

Liquid flow through porous solids occurs in both natural materials, such as rocks and soil, and traditional industrial processes involving water filtration, drainage and petroleum extraction. Man-made solid materials that modulate liquid flow include organic membranes used in phase separation processes and find a wide array of applications. One such application of continuously increasing interest involves the use of Nafion[®] membranes in PEM fuel cells. During normal fuel cell operation, water enters the membrane through sorption and/or diffusion. Variations of water concentration in the membrane result from changes in operating conditions, (e.g., temperature, start-up or shut-down events, circuit load fluctuations). These, in turn, may greatly affect the efficiency of the fuel cell. Indeed, when the water concentration is too high, the two electrodes are flooded and the catalysts are incapacitated, hence retarding (or even completely arresting) the chemical reactions. On the other hand, when the water concentration is too low, the membrane dries up and this limits the conductivity of protons. A parallel issue, on the purely mechanical side, is that Nafion[®] membranes have been experimentally shown to undergo substantial volumetric deformation (swelling) due to changes in water concentration [1,2].

The transport of the liquid phase and its interaction with the solid phase have been studied by different mechanical theories. Among them, mixture theory was one of the earliest to be investigated. This theory was originally proposed by Fick [3], and further refined in a series of subsequent contributions, see, e.g., [4–7]. Adkins [8] and Bowen [9,10] studied flow through porous media using mixture theory. Two major drawbacks of mixture theory are the absence of the liquid volume fraction as a state variable and the need to formulate separate boundary and initial conditions for each phase. The former inhibits the modeling of progressive saturation or drying, while the latter renders the formulation of general initial/boundary-value problems challenging.

An alternative approach involves the use of averaging methods, as advocated, e.g., in [11–14]. Unlike mixture theory, here one introduces the notion of the representative elementary volume (REV), where different parts of the domain are occupied by different phases. Subsequently, the classical balance laws of continuum mechanics are imposed on each phase subject to the requisite interface boundary conditions. This is followed by the derivation of macroscopic balance equations by means of averaging over the REV domain. This approach, while maximally inclusive of the microstructural aspects of the flow, requires an inordinate degree of modeling resolution, and is very challenging for

computational implementation.

A purely continuum approach has been adopted by Coussy [15], who admits porosity as a state variable and formulates separate balance laws for the pure solid and pure liquid phases. This, in turn, necessitates the introduction of separate time derivatives for each phase. The bulk of Coussy’s technical work is predicated on the assumption that the pores of the material are fully saturated. If this is not the case [15, Chapter 6], Coussy introduces a balance between multiple fluid phases (include air) which regulates the porosity of the material. This approach is also explored in [16], where continuum equations of momentum and energy balance are formulated for the whole “mixture”, and are coupled to Darcy’s law-based equations for the diffusion of each phase. The crucial assumption posited in this work is that there is an explicitly known functional dependence of the liquid volume fraction on the capillary pressure and the temperature. With this assumption in place, the governing equations become practical and also amenable to finite element modeling.

In this paper, a new continuum-based theory for the modeling of liquid flow through porous media is proposed and tested by using the finite element method. The proposed theory draws from earlier work, but includes several novelties that are specifically intended to broaden its applicability. Specifically, a key assumption here is that the dry solid and the voids are homogenized into a single macroscopic solid medium. This makes sense for materials in which, regardless of the overall porosity, the size of the pores is much smaller than the overall size of the medium. In this case, the liquid phase contributes additively to macroscopic balance laws without need for separate balances for different phases. Moreover, since the balance laws are stated relative to the (homogenized) solid phase, the proposed theory relies on only one set of material time derivatives, namely those relative to the solid frame. Additionally, the liquid volume fraction is treated as a state variable, thus permitting the imposition of practical boundary conditions and the precise identification of dry, partially saturated, and fully saturated conditions of the porous medium, as well as the transitions from one such condition to another.

The organization of the paper is as follows: Section 2 contains the basic kinematic, kinetic and constitutive assumptions of the theory. This is followed in Section 3 by the statement of the balance laws for the porous medium. Weak forms of these balance laws suitable for finite element implementation are included in Section 4 together with a short discussion on time discretization. Section 5 documents three representative simulations that examine the predictive capacity of the theory. Concluding remarks are offered in Section 6.

2 Concepts, definitions and constitutive relations

Consider a heterogeneous solid body \mathcal{B} consisting of solid matter and voids (pores) of different sizes and shapes. In this work, it is assumed that the characteristic size of the voids is much smaller than the overall size of the body. Therefore, the material possesses a microstructure consisting of solid and void phases, as shown in Figure 1. This microstructure may be locally homogenized to yield a macroscopic continuous solid medium $\bar{\mathcal{B}}$. This medium will be endowed with momentum and density fields, as described below.

2.1 Motion and deformation

Let the continuous solid body $\bar{\mathcal{B}}$ occupy regions \mathcal{R}_0 and \mathcal{R} of volume $\text{vol}(\mathcal{R}_0)$ and $\text{vol}(\mathcal{R})$ at times t_0 and t , respectively. These regions have oriented boundaries $\partial\mathcal{R}_0$ and $\partial\mathcal{R}$, which are assumed smooth enough to possess at every point unique outward unit normals \mathbf{N} and \mathbf{n} , respectively. Also, let \mathbf{X} be the position vector of a point in \mathcal{R}_0 at time t_0 . The motion χ of the macroscopic continuum maps \mathbf{X} to the vector $\mathbf{x} = \chi(\mathbf{X}, t)$ in \mathcal{R} , as in Figure 2. The motion is assumed to be invertible for any given time t . The velocity of a material point occupying \mathbf{x} at time t is subsequently defined as $\mathbf{v}(\mathbf{X}, t) = \frac{\partial\chi(\mathbf{X}, t)}{\partial t}$, where \mathbf{X} is the position of the same material point at t_0 . Likewise, the deformation gradient at a point \mathbf{x} in \mathcal{R} relative to its image \mathbf{X} in \mathcal{R}_0 is defined as $\mathbf{F}(\mathbf{X}, t) = \frac{\partial\chi(\mathbf{X}, t)}{\partial\mathbf{X}}$. Since the motion is invertible, $J = \det(\mathbf{F}) \neq 0$ for all (\mathbf{X}, t) , and without loss of generality, it is further assumed that $J > 0$.

2.2 Porosity, liquid volume fraction and density

The porosity of a solid is generally defined as the ratio of the volume of voids over the total volume of the porous solid. A local definition of porosity at the macroscale requires the introduction of a representative element of volume $dv \ll \text{vol}(\mathcal{R})$ which accurately resolves the microscopic poral structure of the material. Therefore, the size of dv should be significantly larger than the average size of the pores. Now, the porosity $\bar{\phi}$ of a solid at a macroscopic point may be defined as the ratio of the void volume to the volume dv of the porous solid in the representative element. It follows that, under all circumstances, $0 \leq \bar{\phi} < 1$. **It is assumed in this work that changes in the porosity $\bar{\phi}$ due to the deformation of the solid are negligible.**

Some or all of the pores may be filled with a liquid, rendering the body partially or fully saturated (otherwise, it is referred to as dry). In a partially saturated solid, a fraction

of the voids is occupied (either partially or fully) by the liquid, as in Figure 3. Specifically, assume that the volume of the liquid in the representative element is dv_l . Now, the liquid volume fraction ϕ is defined locally in the macroscale by

$$dv_l = \phi dv , \quad (1)$$

where $\phi \leq \bar{\phi}$, with the strict equality holding for the fully saturated case.

Mass conservation in the microscale implies that the macroscopic mass density ρ satisfies the condition

$$\rho dv = \rho_l dv_l + \rho_s dv , \quad (2)$$

where ρ_l and ρ_s are the densities of the pure liquid and the (dry) porous solid, respectively. Here, ρ_s is a homogenized density which accounts for the presence of voids in the solid.

Equations (1) and (2) now imply that

$$\rho = \rho_l \phi + \rho_s . \quad (3)$$

2.3 Liquid mass flux and linear momentum

Preliminary to the definition of liquid mass flux, let \mathbf{v}_l be the velocity of the liquid phase, which, in general, differs from the velocity of the macroscopic solid. Now, the flux of liquid mass through the solid can be expressed as

$$\mathbf{q} = \rho_l \phi \mathbf{v}^r , \quad (4)$$

where $\mathbf{v}^r = \mathbf{v}_l - \mathbf{v}$ is the relative velocity of liquid. Taking into account (3) and (4), the linear momentum $\rho_s \mathbf{v} + \rho_l \phi \mathbf{v}_l$ of the solid and liquid phases may be written as

$$\rho_s \mathbf{v} + \rho_l \phi \mathbf{v}_l = \rho \mathbf{v} + \mathbf{q} . \quad (5)$$

When the material is not fully-saturated, it is assumed that the flux of liquid mass obeys Fick's law [3]. Indeed, this stipulates that the flux of the liquid mass is proportional to the effective liquid density $\rho_l \phi$ and to the gradient of the liquid volume fraction, that is,

$$\mathbf{q} = -K \rho_l \phi \text{grad } \phi , \quad (6)$$

where $K(> 0)$ is an isotropic diffusivity parameter.

Equations (4) and (6) permit the representation of the liquid velocity \mathbf{v}_l as a function of the velocity \mathbf{v} of the macroscopic solid and the spatial gradient $\text{grad } \phi$ of the liquid volume fraction according to

$$\mathbf{v}_l = \mathbf{v} - K \text{grad } \phi . \quad (7)$$

Therefore, if the densities ρ_s, ρ_l , the velocity \mathbf{v} and the liquid volume fraction ϕ are adopted as state variables in this theory, the preceding observation implies that the liquid velocity \mathbf{v}_l is not an independent state variable. **This is an important point of difference from classical mixture theory, as the latter requires the use of velocities for both the solid and the liquid phase.**

2.4 Effective stress

The macroscopic solid and the liquid contribute to the stress in the body. Here, the cumulative Cauchy stress is assumed to take the form

$$\mathbf{T} = \mathbf{T}_s - p_l \mathbf{i} , \quad (8)$$

where \mathbf{T}_s is the stress for the macroscopic solid, p_l is the excess pressure due to the presence of the liquid phase, and \mathbf{i} is the spatial second-order identity tensor. Similar additivity assumptions for stress have been previously utilized in [16–18].

In this work, the solid response is assumed hyperelastic. For specificity **and given the moderate magnitude of the deformation**, the solid is taken to obey the Kirchhoff-Saint Venant constitutive law, according to which the second Piola-Kirchhoff stress $\mathbf{S}_s = J\mathbf{F}^{-1}\mathbf{T}_s\mathbf{F}^{-T}$ is given by

$$\mathbf{S}_s = \lambda \operatorname{tr}(\mathbf{E})\mathbf{I} + 2\mu\mathbf{E} . \quad (9)$$

Here, \mathbf{E} is the Lagrangian strain, while λ, μ are elastic constants for the macroscopic solid.

The excess pressure due to the liquid phase should clearly depend on the liquid volume fraction, that is $p_l = \hat{p}_l(\phi)$. For simplicity, a linear relation is assumed here in the form

$$p_l = C\phi , \quad (10)$$

where C is a material constant (see [16] for a related assumption).

3 Balance laws

Consider a part of the macroscopic solid, which occupies an arbitrary closed and bounded region $\mathcal{P} \subset \mathcal{R}$ with smooth boundary $\partial\mathcal{P}$ at time t .

Balance of mass and linear momentum are formulated below by examining the material in region \mathcal{P} . Here, all material time derivatives of integrals over \mathcal{P} are defined by keeping

material particles of the macroscopic solid fixed. Therefore, the material time derivatives of arbitrary scalar and vector functions $\psi(\mathbf{x}, t)$ and $\mathbf{w}(\mathbf{x}, t)$ are given by

$$\frac{d\psi}{dt} = \frac{\partial\psi}{\partial t} + \text{grad } \psi \cdot \mathbf{v} \quad , \quad \frac{d\mathbf{w}}{dt} = \frac{\partial\mathbf{w}}{\partial t} + (\text{grad } \mathbf{w})\mathbf{v} . \quad (11)$$

3.1 Balance of mass

The rate of change of total mass for the region \mathcal{P} occupied by the macroscopic solid at time t takes the form

$$\frac{d}{dt} \int_{\mathcal{P}} \rho \, dv = \frac{d}{dt} \int_{\mathcal{P}} \rho_s \, dv + \frac{d}{dt} \int_{\mathcal{P}} \rho_l \phi \, dv , \quad (12)$$

where use is made of (3). Since the mass of the macroscopic solid material is conserved, the preceding equation readily reduces to

$$\frac{d}{dt} \int_{\mathcal{P}} \rho \, dv = \frac{d}{dt} \int_{\mathcal{P}} \rho_l \phi \, dv . \quad (13)$$

Also, since all changes of the liquid mass in \mathcal{P} are due to the flux of the liquid \mathbf{q} at the boundary $\partial\mathcal{P}$, it follows from (13) that the balance of total mass may be expressed simply as

$$\frac{d}{dt} \int_{\mathcal{P}} \rho_l \phi \, dv = - \int_{\partial\mathcal{P}} \mathbf{q} \cdot \mathbf{n} \, da . \quad (14)$$

Appealing to the Reynolds' transport, divergence and localization theorems, the integral statement (14) gives rise to a corresponding local statement, which is given by

$$\frac{d}{dt}(\rho_l \phi) + \rho_l \phi \, \text{div } \mathbf{v} = - \text{div } \mathbf{q} . \quad (15)$$

Alternatively, combining (13) and (14), mass balance may be expressed in term of the macroscopic mass density as

$$\frac{d\rho}{dt} + \rho \, \text{div } \mathbf{v} = - \text{div } \mathbf{q} . \quad (16)$$

In comparing equation (16) to the corresponding mass balance equation in classical mixture theory, it is noted that the latter is obtained by summing the respective balance equations for the different phases and defining an equivalent material time derivative as a linear combination of the density-weighted derivatives of the individual phases. Clearly, no such summation is needed here, because the mass balance equation is written with respect to the macroscopic solid and, hence, incorporates changes to the fluid mass through the flux term \mathbf{q} .

The conventional local form of mass balance is recovered from (16) by merely setting $\mathbf{q} = \mathbf{0}$.

3.2 Balance of linear momentum

Balance of linear momentum necessitates that the rate of change of total linear momentum for the region \mathcal{P} occupied by the macroscopic solid at time t be equal to the external forces acting on the material and the flux of linear momentum $-(\rho_l \phi \mathbf{v}_l) \mathbf{v}^r \cdot \mathbf{n}$ through the boundary $\partial \mathcal{P}$. This translates to

$$\frac{d}{dt} \int_{\mathcal{P}} (\rho_s \mathbf{v} + \rho_l \phi \mathbf{v}_l) dv = \int_{\mathcal{P}} \rho \mathbf{b} dv + \int_{\partial \mathcal{P}} \mathbf{t} da - \int_{\partial \mathcal{P}} (\rho_l \phi \mathbf{v}_l) \mathbf{v}^r \cdot \mathbf{n} da, \quad (17)$$

where $\mathbf{t} = \mathbf{T} \mathbf{n}$ is the traction vector on $\partial \mathcal{P}$. Recalling (4) and (5), the preceding equation may be equivalently rewritten as

$$\frac{d}{dt} \int_{\mathcal{P}} (\rho \mathbf{v} + \mathbf{q}) dv = \int_{\mathcal{P}} \rho \mathbf{b} dv + \int_{\partial \mathcal{P}} \mathbf{t} da - \int_{\partial \mathcal{P}} (\mathbf{q} \cdot \mathbf{n}) \mathbf{v}_l da. \quad (18)$$

Invoking, again, the Reynolds' transport theorem and also the mass balance equation (16) and the divergence theorem, the integral statement of linear momentum (18) may be recast in the form

$$\int_{\mathcal{P}} \left(\rho \frac{d\mathbf{v}}{dt} - \mathbf{v} \operatorname{div} \mathbf{q} + \frac{d\mathbf{q}}{dt} + \mathbf{q} \operatorname{div} \mathbf{v} \right) dv = \int_{\mathcal{P}} \rho \mathbf{b} dv + \int_{\mathcal{P}} \operatorname{div} \mathbf{T} dv - \int_{\mathcal{P}} \operatorname{div} (\mathbf{v}_l \otimes \mathbf{q}) dv. \quad (19)$$

The corresponding local form follows readily from (19), and reads

$$\rho \frac{d\mathbf{v}}{dt} - \mathbf{v} \operatorname{div} \mathbf{q} + \frac{d\mathbf{q}}{dt} + \mathbf{q} \operatorname{div} \mathbf{v} = \rho \mathbf{b} + \operatorname{div} \mathbf{T} - \operatorname{div} (\mathbf{v}_l \otimes \mathbf{q}). \quad (20)$$

Again, setting $\mathbf{q} = \mathbf{0}$ reduces (20) to the conventional local form of linear momentum balance.

4 Finite element implementation

4.1 Weak forms

In this section, weak counterparts of the local balance equations (15) and (20) are constructed preliminary to finite element discretization.

For mass balance, equation (15) is first weighted by a scalar test function η , then integrated over \mathcal{P} , so that, upon invoking integration by parts and the divergence theorem, it leads to

$$\int_{\mathcal{P}} \eta \rho_l \frac{d\phi}{dt} dv + \int_{\mathcal{P}} \eta \rho_l \phi \operatorname{div} \mathbf{v} dv - \int_{\mathcal{P}} \operatorname{grad} \eta \cdot \mathbf{q} dv + \int_{\partial \mathcal{P}} \eta \mathbf{q} \cdot \mathbf{n} da = 0. \quad (21)$$

Likewise, for balance of linear momentum, equation (20) is contracted with an arbitrary vector test function $\boldsymbol{\xi}$ and integrated over the domain \mathcal{P} . This leads to

$$\begin{aligned} \int_{\mathcal{P}} \boldsymbol{\xi} \cdot \rho \frac{d\mathbf{v}}{dt} dv - \int_{\mathcal{P}} \boldsymbol{\xi} \cdot \mathbf{v} \operatorname{div} \mathbf{q} dv + \int_{\mathcal{P}} \boldsymbol{\xi} \cdot \frac{d\mathbf{q}}{dt} dv + \int_{\mathcal{P}} \boldsymbol{\xi} \cdot \mathbf{q} \operatorname{div} \mathbf{v} dv - \int_{\mathcal{P}} \boldsymbol{\xi} \cdot \rho \mathbf{b} dv \\ - \int_{\mathcal{P}} \boldsymbol{\xi} \cdot \operatorname{div} \mathbf{T} dv + \int_{\mathcal{P}} \boldsymbol{\xi} \cdot \mathbf{v}_l \operatorname{div} \mathbf{q} dv + \int_{\mathcal{P}} \boldsymbol{\xi} \cdot [(\operatorname{grad} \mathbf{v}_l) \mathbf{q}] dv = 0. \end{aligned} \quad (22)$$

Applying integration by parts and the divergence theorem to the second and sixth terms on the left-hand side of (22), one may recast the preceding weak form as

$$\begin{aligned} \int_{\mathcal{P}} \boldsymbol{\xi} \cdot \rho \frac{d\mathbf{v}}{dt} dv + \int_{\mathcal{P}} [(\operatorname{grad} \boldsymbol{\xi}) \mathbf{q}] \cdot \mathbf{v} dv + \int_{\mathcal{P}} \boldsymbol{\xi} \cdot [(\operatorname{grad} \mathbf{v}) \mathbf{q}] dv - \int_{\partial \mathcal{P}} [(\boldsymbol{\xi} \cdot \mathbf{v}) \mathbf{q}] \cdot \mathbf{n} da \\ + \int_{\mathcal{P}} \boldsymbol{\xi} \cdot \frac{d\mathbf{q}}{dt} dv + \int_{\mathcal{P}} \boldsymbol{\xi} \cdot \mathbf{q} \operatorname{div} \mathbf{v} dv - \int_{\mathcal{P}} \boldsymbol{\xi} \cdot \rho \mathbf{b} dv + \int_{\mathcal{P}} \operatorname{grad} \boldsymbol{\xi} \cdot \mathbf{T} dv - \int_{\partial \mathcal{P}} \boldsymbol{\xi} \cdot \mathbf{t} da \\ + \int_{\mathcal{P}} \boldsymbol{\xi} \cdot \mathbf{v}_l \operatorname{div} \mathbf{q} dv + \int_{\mathcal{P}} \boldsymbol{\xi} \cdot [(\operatorname{grad} \mathbf{v}_l) \mathbf{q}] dv = 0. \end{aligned} \quad (23)$$

The last two terms on the left-hand side of (23) may be further rewritten with the aid of integration by parts and the divergence theorem as

$$\int_{\mathcal{P}} \boldsymbol{\xi} \cdot \mathbf{v}_l \operatorname{div} \mathbf{q} dv + \int_{\mathcal{P}} \boldsymbol{\xi} \cdot [(\operatorname{grad} \mathbf{v}_l) \mathbf{q}] dv = \int_{\partial \mathcal{P}} [(\boldsymbol{\xi} \cdot \mathbf{v}_l) \mathbf{q}] \cdot \mathbf{n} da - \int_{\mathcal{P}} [(\operatorname{grad} \boldsymbol{\xi}) \mathbf{q}] \cdot \mathbf{v}_l dv. \quad (24)$$

This leads to an alternative expression for the weak form of linear momentum balance as

$$\begin{aligned} \int_{\mathcal{P}} \boldsymbol{\xi} \cdot \rho \frac{d\mathbf{v}}{dt} dv + \int_{\mathcal{P}} [(\operatorname{grad} \boldsymbol{\xi}) \mathbf{q}] \cdot (K \operatorname{grad} \phi) dv + \int_{\mathcal{P}} \boldsymbol{\xi} \cdot [(\operatorname{grad} \mathbf{v}) \mathbf{q}] dv \\ + \int_{\mathcal{P}} \boldsymbol{\xi} \cdot \frac{d\mathbf{q}}{dt} dv + \int_{\mathcal{P}} \boldsymbol{\xi} \cdot \mathbf{q} \operatorname{div} \mathbf{v} dv - \int_{\mathcal{P}} \boldsymbol{\xi} \cdot \rho \mathbf{b} dv + \int_{\mathcal{P}} \operatorname{grad} \boldsymbol{\xi} \cdot \mathbf{T} dv \\ - \int_{\partial \mathcal{P}} \boldsymbol{\xi} \cdot \mathbf{t} da - \int_{\partial \mathcal{P}} [(\boldsymbol{\xi} \cdot (K \operatorname{grad} \phi)) \mathbf{q}] \cdot \mathbf{n} da = 0, \end{aligned} \quad (25)$$

where the liquid velocity is eliminated by using (7).

4.2 Space and time discretization

The finite element approximation is based on the weak forms (21) and (25). Appealing to the arbitrariness of the test functions $\boldsymbol{\xi}$ and η , these lead to a coupled system of integro-differential equations with the macroscopic solid displacement \mathbf{u} and liquid volume fraction ϕ as unknowns. A standard semi-discretization method is employed for the solution of (21) and (25), where the spatial discretization of \mathbf{u} and ϕ is effected using a standard displacement-like formulation. This, in turn, gives rise to a coupled system of first- and

second-order ordinary partial differential equations in time. These are subsequently integrated in a typical time interval $(t_n, t_{n+1}]$ using an implicit Newmark scheme [19], such that

$$\begin{aligned} \mathbf{u}_{n+1} &= \mathbf{u}_n + \mathbf{v}_n \Delta t_n + \frac{1}{2} \left[(1 - 2\beta) \frac{d\mathbf{v}}{dt} \Big|_n + 2\beta \frac{d\mathbf{v}}{dt} \Big|_{n+1} \right] \Delta t_n^2 \\ \mathbf{v}_{n+1} &= \mathbf{v}_n + \left[(1 - \gamma) \frac{d\mathbf{v}}{dt} \Big|_n + \gamma \frac{d\mathbf{v}}{dt} \Big|_{n+1} \right] \Delta t_n \\ \phi_{n+1} &= \phi_n + \left[(1 - \gamma) \frac{d\phi}{dt} \Big|_n + \gamma \frac{d\phi}{dt} \Big|_{n+1} \right] \Delta t_n, \end{aligned} \quad (26)$$

where $(\cdot)_n = (\cdot)|_n = (\cdot)(t_n)$, $\Delta t_n = t_{n+1} - t_n$, and β, γ are the Newmark parameters.

The resulting nonlinear algebraic equations are solved with the Newton-Raphson method. This requires consistent linearization of the weak forms with respect to \mathbf{u} and ϕ , which is derived in the Appendix.

5 Numerical simulations

The finite element formulation of the model described in Section 4 was implemented in the general-purpose nonlinear program FEAP [20,21]. The model and its numerical implementation were tested on three representative simulations discussed below. All simulations employed 8-node isoparametric brick elements with full $2 \times 2 \times 2$ Gaussian quadrature. In addition, the time integration parameters defined in Section 4.2 were set to $\beta = 0.25$ and $\gamma = 0.5$.

The material properties in the simulations were chosen for Nafion[®], which is suitable for modeling within the proposed theory, owing to the small size of its pores (with diameter of 20–30 nm [22]) compared to the typical thickness of industrial Nafion[®] membranes (0.175 mm [23]). The Nafion[®] properties were set to: $(\lambda, \mu) = (0.40 \times 10^7, 0.27 \times 10^7)$ Pa [24], $\rho_s = 2 \times 10^3$ kgr/m³ [24], $\rho_l = 10^3$ kgr/m³, $\bar{\phi} = 0.4$ [25], $K = 1.0 \times 10^{-10}$ m²/s [26], and $C = 10^6$ Pa. The last parameter was chosen heuristically such that the liquid excess pressure p_l in (10) be in the range of one atmosphere at saturation.

5.1 Stretching of a saturated cube

A 0.5 mm cube made of saturated Nafion[®] is stretched uniformly using displacement control on one face while being fixed on the opposite face and free on all four lateral faces. Zero liquid flux boundary conditions are enforced on the whole boundary. The imposed

stretching is applied at time $t = 0$ and the body is subsequently allowed to reach steady-state.

A uniform $10 \times 5 \times 5$ mesh is used to discretize the problem, with the finer resolution aligned with the direction of stretching (here, the x -direction). Also, time integration is performed with constant step-size $\Delta t = 10^{-6}$ s.

Figure 4 shows the distribution of the liquid volume fraction along the centerline of the cube in the x -direction at three different times and for stretch $\lambda = 0.1$. At $t = 10^{-6}$ s, the body is essentially saturated away from the stretched end, while near this end its liquid volume fraction exhibits a precipitous drop. At $t = 10^{-5}$ s, the distribution of the liquid volume fraction is much smoother reflecting the flow of liquid toward the stretched end of the body, while at $t = 10^{-4}$ s the volume fraction is spatially uniform and below the saturation limit due to the attainment of steady-state.

Next, the cube is stretched in increments of $\Delta\lambda = 0.1$ up to a total stretch of $\lambda = 0.4$. After each stretch increment, the body is allowed to reach steady-state before the next increment is imposed. The relation between the liquid volume fraction at steady-state and the stretch is illustrated in Figure 5 and shows the expected monotonic decrease. The same figure also depicts the total volume of the liquid, which remains constant throughout the stretch loading owing to the zero-flux boundary conditions.

5.2 Squeezing of a saturated cube

A 0.5 mm cube of saturated Nafion[®] is compressed uniformly on one of its faces using displacement control, while the opposite face remains fixed and each of the four lateral faces is free to slide on its own plane only. The liquid may escape from the compressed face, while all other faces are assumed to be impermeable. The block is initially squeezed to $\lambda_s = 93\%$ while keeping the liquid volume fraction to the saturation value of $\phi = 0.4$ on the compressed face. Then, it is stretched back to its original shape, where it is kept until the liquid volume fraction reaches steady state. During the stretching and until steady state is attained, the compressed face is subject to zero liquid flux conditions. Each of three loading stages is imposed proportionally over a period of 0.1 s.

A uniform $5 \times 5 \times 5$ mesh is used in this problem and the time step-size is set to 1 ms. As illustrated in Figure 6, the total volume of the liquid decreases during squeezing, then remains constant while the body returns to its original configuration. At the same time, the total volume of the porous medium initially decreases and then increases back to its original value.

The same block is subsequently subjected to repeated squeezing and stretching of the same magnitude and rate as before. In this case, liquid escapes from the solid block repeatedly until the solid material pushes enough of it out of the block to reach a steady state of liquid volume fraction. To prevent back-flow into the block, the fixed liquid volume fraction boundary condition on the compressed face during squeezing is chosen to be equal to the minimum of the current steady-state liquid volume fraction and the asymptotic liquid volume fraction ϕ_a at maximum squeezing. The latter is equal, in this case, to

$$\phi_a = \frac{\lambda_s V - (1 - \bar{\phi})V}{\lambda_s V} = \frac{0.93 - (1 - 0.4)}{0.93} \doteq 0.35, \quad (27)$$

where V denotes the initial volume of the block. The preceding definition is predicated upon the assumption that the solid matter (being hyperelastic) returns to its original volume when the liquid volume reaches a steady value after a sufficient number of squeezes. The results of this numerical simulation are illustrated in Figure 7, where it is specifically shown that this steady volume of liquid is reached after only three successive squeezes.

5.3 Flexure of a Nafion[®] film due to water absorption

It has been experimentally observed that when placing a water droplet on a dry thin film made of Nafion[®], the region surrounding the droplet initially exhibits a bulge, which later disappears as the water evaporates and/or is diffused into the film [2]. To simulate this experiment, a water droplet is idealized by means of a prescribed liquid volume fraction boundary condition on a square region with 3 mm side at the center of the top surface of a $10 \times 10 \times 0.125$ mm Nafion[®] block. The latter is fixed on all of its four lateral faces and zero liquid flux boundary condition is imposed on all boundaries except for the droplet region. The supply of water is terminated at $t = 450$ s, at which time the Dirichlet boundary condition $\phi = \bar{\phi}$ on the droplet region is replaced by a corresponding **zero** liquid flux condition. No attempt is made here to account for evaporation.

A uniform $20 \times 20 \times 5$ mesh is used for the analysis, and symmetry is exploited in modeling only a quarter of the domain. Also, the time step-size is set to 0.2 s.

Figure 8 illustrates the flexure of the film at the center of water droplet **for three different values of the liquid pressure constant C of equation (10)**. This is done to explore the predictive range of this variable, which, as stated earlier, is chosen without direct experimental evidence. It is noted that maximum flexure **in the range of approximately 0.35 mm to 0.51 mm is achieved at $t = 450$ s**. After the water supply is terminated, the flexure starts decreasing with time. **As seen in Figure 8, the maximum flexure increases**

with C , but the rate of its decrease after $t = 450$ sec appears to be independent of C . A contour plot of the transverse displacement at $t = 450$ s is illustrated in Figure 9 on the deformed configuration. These results are both qualitatively and quantitatively consistent with the experimental findings in [2], although the rate of decrease in the maximum flexure appears to be significantly slower in the simulations.

6 Conclusions

The principal goal of this study is to enable the modeling of liquid flow in elastic porous solids undergoing finite deformation in the presence of time- and space-varying liquid concentration. The proposed continuum-mechanical model satisfies the preceding imperatives, while allowing for the imposition of meaningful boundary conditions on displacement and liquid concentration. In addition, the model lends itself to straightforward and relatively efficient implementation using the finite element method. On the latter point, the choice of state variables leads to only one extra degree of freedom (the liquid volume fraction) per node, since the proposed formulation of the governing equations results in the elimination of the liquid velocity from the system of equations. Further, treating the liquid volume fraction as state variable facilitates the tracking of the liquid flow and permits the identification of regions of dry, partial or full saturation.

The numerical simulations on Nafion[®] demonstrate the predictive power of the proposed model and its intuitively correct response to simple loading conditions, such as stretching and squeezing under saturated conditions. In particular, the stretching simulation shows that the liquid redistributes itself in the pores at a lower concentration by conserving the total liquid mass. Likewise, the squeezing simulation demonstrates that liquid exits the porous solid leading to a lower asymptotic uniform concentration. Also, the proposed model captures the flexure of a Nafion[®] film caused by a droplet of water on top surface, and even provides quantitatively correct for both maximum flexure and time to achieve the maximum flexure.

There exist still two items that merit further attention in connection with the proposed model. First, the constitutive relation between liquid pressure and liquid volume fraction is postulated to be linear and may not adequately represent the actual physics, especially when the porous solid is close to full saturation. Second, the porosity is taken to be independent of deformation, which may not be accurate under very large deformations. Both items will be addressed in subsequent work.

Acknowledgments

This work was supported in part by an Academic Excellence Alliance grant awarded by the KAUST Office of Competitive Research Fund under the title “An Integrated Theoretical and Computational Study of Certain Mechanical and Chemical Properties of Nafion Membranes”.

Appendix: Consistent Linearization of the Balance Laws

In this appendix, expressions are recorded for the consistent element tangent stiffness matrix required by the Newton-Raphson method to determine the nodal displacements and pressures from the weak forms (21) and (25) in conjunction with the time integration equations (26). To this end, let the element interpolations at time t_{n+1} be given by $\mathbf{u}_{n+1} = \sum_{I=1}^N N_I \hat{\mathbf{u}}_{I_{n+1}}$, $\phi_{n+1} = \sum_{I=1}^N N_I \hat{\phi}_{I_{n+1}}$, $\boldsymbol{\xi}_{n+1} = \sum_{J=1}^N N_J \hat{\boldsymbol{\xi}}_{J_{n+1}}$, $\eta_{n+1} = \sum_{J=1}^N N_J \hat{\eta}_{J_{n+1}}$, where N_I , $I = 1, 2, \dots, N$, denote the I -th element interpolation function and the superscript “ $(\hat{\cdot})_I$ ” signifies the value of a variable (\cdot) at node I . For brevity, the subscript $n+1$ is suppressed in the remainder of the appendix.

The linearization of the weak forms (21) and (25) for a typical element e gives rise to a tangent stiffness matrix of the form

$$[K] = \begin{bmatrix} [K^{\phi u}] & [K^{\phi \phi}] \\ [K^{uu}] & [K^{u\phi}] \end{bmatrix}, \quad (\text{A.1})$$

where the $N \times 3N$ submatrix $[K^{\phi u}]$ and the $N \times N$ submatrix $[K^{\phi \phi}]$ result from the linearization of the mass balance equation (21) in the direction of $\hat{\mathbf{u}}$ and $\hat{\phi}$, respectively. Likewise, the $3N \times 3N$ submatrix $[K^{uu}]$ and the $3N \times N$ submatrix $[K^{u\phi}]$ are due to the linearization of the momentum balance equation (25) along the same directions.

Taking into account (21) and (26), it can be easily shown that

$$K_{I(jJ)}^{\phi u} = \frac{\gamma}{\beta \Delta t} \int_{\Omega^e} \rho_l \phi N_I N_{J,j} dv \quad (\text{A.2})$$

and

$$K_{IJ}^{\phi \phi} = \frac{1}{\gamma \Delta t} \int_{\Omega^e} \rho_l N_I N_J dv + \int_{\Omega^e} \rho_l N_I N_J \operatorname{div} \mathbf{v} dv + \int_{\Omega^e} K \rho_l \sum_{k=1}^3 (N_{I,k} (\phi N_{J,k} + N_J \phi_{,k})) dv, \quad (\text{A.3})$$

where $j, k = 1, 2, 3$ are spatial coordinate indices, $N_{I,j}$ is the partial derivative of N_I with respect to the spatial coordinate x_j , and Ω^e is the element domain.

Correspondingly, starting from (25) and (26), it is found that

$$K_{(iI)(jJ)}^{uu} = \frac{1}{\beta\Delta t^2} \int_{\Omega^e} N_I \rho N_J \delta_{ij} dv + \frac{\gamma}{\beta\Delta t} \int_{\Omega^e} \left(\sum_{k=1}^3 N_I q_k N_{J,k} \right) \delta_{ij} dv + \frac{\gamma}{\beta\Delta t} \int_{\Omega^e} N_I q_i N_{J,j} dv + K_{(iI)(jJ)}^m \quad (\text{A.4})$$

and

$$K_{(iI)J}^{u\phi} = \int_{\Omega^e} N_I \rho_l N_J \frac{dv_i}{dt} dv + \int_{\Omega^e} K \sum_{k=1}^3 (-K \rho_l \phi_{,i} N_{I,k} (N_J \phi_{,k} + \phi N_{J,k}) + N_{I,i} N_{J,k} q_k) dv - \int_{\Omega^e} K \rho_l N_I \sum_{k=1}^3 (v_{i,k} (\phi N_{J,k} + N_J \phi_{,k})) dv - \int_{\Omega^e} K \rho_l N_I (\phi N_{J,i} + N_J \phi_{,i}) \text{div } \mathbf{v} dv - \int_{\Omega^e} K \rho_l N_I \left(N_J \frac{d\phi_{,i}}{dt} + \frac{1}{\gamma\Delta t} \phi N_{J,i} + \frac{1}{\gamma\Delta t} N_I \phi_{,i} + \frac{d\phi}{dt} N_{J,i} \right) dv, \quad (\text{A.5})$$

where $i, j, k = 1, 2, 3$ are spatial coordinate indices. Also, $K_{(iI)(jJ)}^m$ denotes the material tangent stiffness emanating from the stress-divergence term in (25).

References

- [1] J.A. Elliott, S. Hanna, A.M.S. Elliott, and G.E. Cooley. The swelling behaviour of perfluorinated ionomer membranes in ethanol/water mixtures. *Polymer*, 42:2251–2253, 2001.
- [2] S. Goswami, S. Klaus, and J.B. Benziger. Wetting and absorption of water drops on Nafion films. *Langmuir*, 24(16):8627–8633, 2008.
- [3] A. Fick. On liquid diffusion. *Philosophical Magazine*, 10(63):30–39, 1855.
- [4] A.E.Green and P.M.Naghdi. A theory of mixtures. *Archive for Rational Mechanics and Analysis*, 24:243–263, 1967.
- [5] A.E.Green and P.M.Naghdi. On basic equations of mixture. *Quarterly Journal of Mechanics and Applied Mathematics*, 22:427–438, 1969.
- [6] R.J. Atkin and R.E. Craine. Continuum theories of mixtures: Basic theory and historical development. *Quarterly Journal of Mechanics and Applied Mathematics*, 29:209–244, 1976.
- [7] K.R. Rajagopal and L. Tao. *Mechanics of Mixture*. World Properties, Singapore, 1995.
- [8] J.E. Adkins. Non-linear diffusion: III. Diffusion through isotropic highly elastic solids. *Philosophical Transactions of the Royal Society A*, 256:301–316, 1964.

- [9] R.M. Bowen. Incompressible porous media models by use of the theory of mixtures. *International Journal of Engineering Science*, 18:1129–1148, 1980.
- [10] R.M. Bowen. Compressible porous media models by use of the theory of mixtures. *International Journal of Engineering Science*, 20:697–735, 1982.
- [11] S.M. Hassanizadeh and W.G. Gray. General conservation equations for multiphase systems: 1. Averaging procedure. *Advances in Water Resources*, 2(4):131–144, 1979.
- [12] S.M. Hassanizadeh and W.G. Gray. General conservation equations for multiphase systems: 2. Mass, momenta, energy and entropy. *Advances in Water Resources*, 2(4):191–203, 1990.
- [13] S.M. Hassanizadeh and W.G. Gray. General conservation equations for multiphase systems:3. Constitutive theory for porous media flow. *Advances in Water Resources*, 3:25–40, 1980.
- [14] Y. Bachmat and J. Bear. Macroscopic modelling of transport phenomena in porous media. 1: The continuum approach. *Transport in Porous Media*, 21:213–240, 1986.
- [15] O. Coussy. *Poromechanics*. John Wiley and Sons, Chichester, 2004.
- [16] D. Gawin, P. Baggio, and B.A. Schrefler. Coupled heat, water and gas flow in deformable porous media. *International Journal for Numerical Methods in Fluids*, 20(E2):969–987, 1995.
- [17] J. Korsawe, G. Starke, W. Wang, and O. Kolditz. Finite element analysis of poro-elastic consolidation in porous media: standard and mixed approaches. *Computer Methods in Applied Mechanics and Engineering*, 195:1096–1115, 2006.
- [18] J. Ghaboussi and E.L. Wilson. Flow of compressible fluid in porous elastic media. *International Journal for Numerical Methods in Engineering*, 5:419–442, 1973.
- [19] N.M. Newmark. A method of computation in structural dynamics. *ASCE Journal of Engineering Mechanics*, 85:67–94, 1959.
- [20] R.L. Taylor. *FEAP - A Finite Element Analysis Program, User Manual*. University of California, Berkeley. <http://www.ce.berkeley.edu/feap>.
- [21] R.L. Taylor. *FEAP - A Finite Element Analysis Program, Programmer Manual*. University of California, Berkeley. <http://www.ce.berkeley.edu/feap>.
- [22] D.J. Gargas, D.A. Bussian, and S.K. Buratto. Investigation of connectivity of hydrophilic domains in Nafion using electrochemical pore-directed nanolithography. *Nano Letters*, 5:2184–2187, 2005.
- [23] K.A. Mauritz and R.B. Moore. State of understanding of Nafion. *Chemical Reviews*, 104:4535–4586, 2004.
- [24] M.B. Satterfield, P.W. Mjsztrik, H. Ota, J.B. Benziger, and A.B. Bocarsly. Mechanical properties of Nafion and Titania/Nafion composite membranes for polymer electrolyte membrane fuel cells. *Journal of Polymer Science Part B: Polymer Physics*, 44(16):2327–2345, 2006.

- [25] S. Song, W. Zhou, J. Tian, and R. Cai. Ethanol crossover phenomena and its influence on performance of DEFC. *Journal of Power Sources*, 145:266–271, 2005.
- [26] S. Motupally, A.J. Becker, and J.W. Weidner. Diffusion of water in Nafion 115 membranes. *Journal of the Electrochemical Society*, 147:3171–3177, 2000.

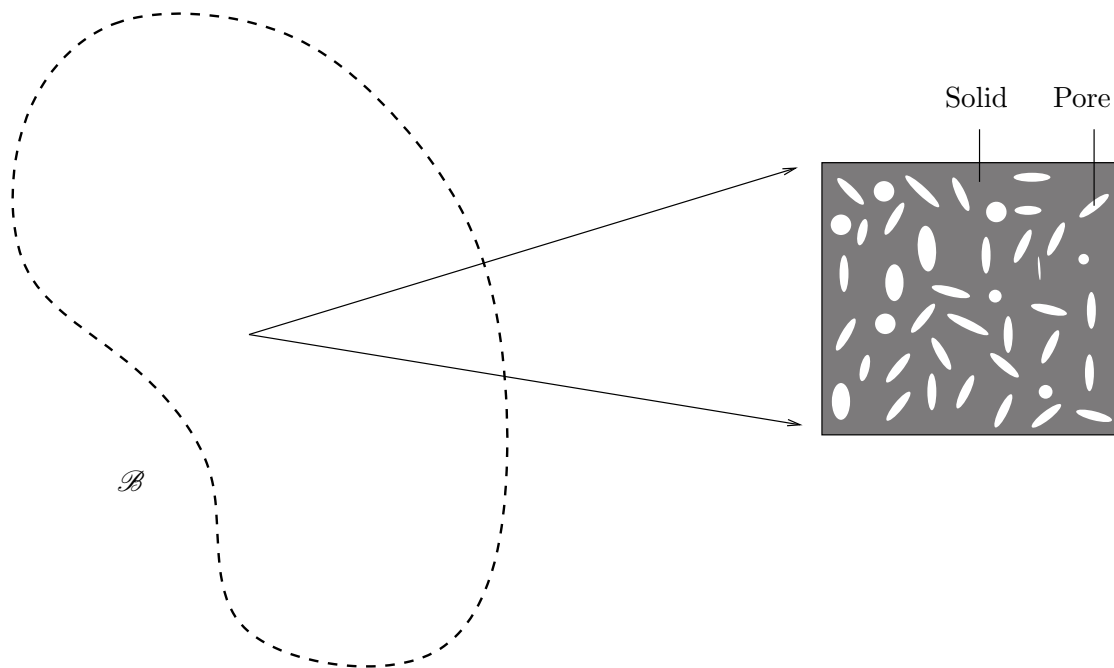


Figure 1: Multiscale modeling and homogenization

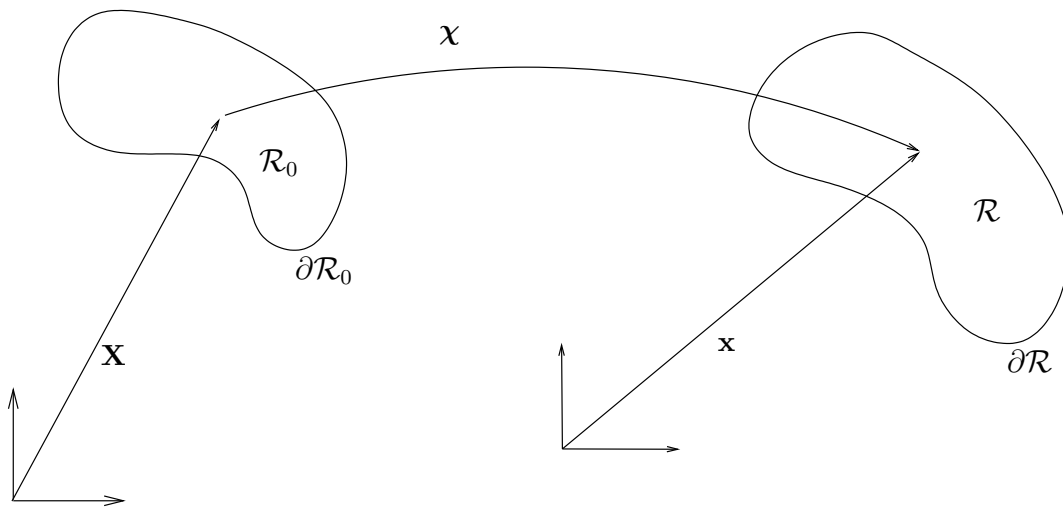


Figure 2: Motion of homogenized body

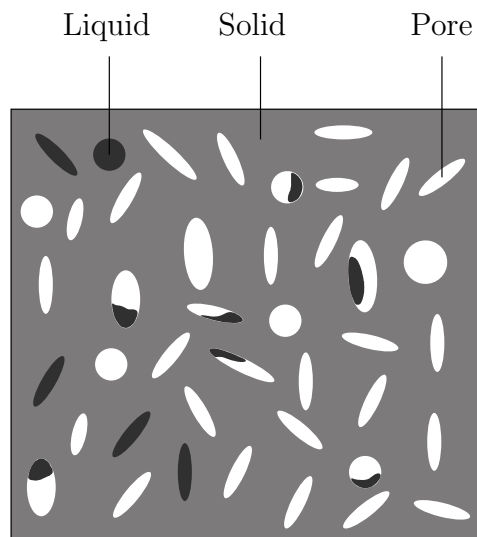


Figure 3: Partially saturated porous medium

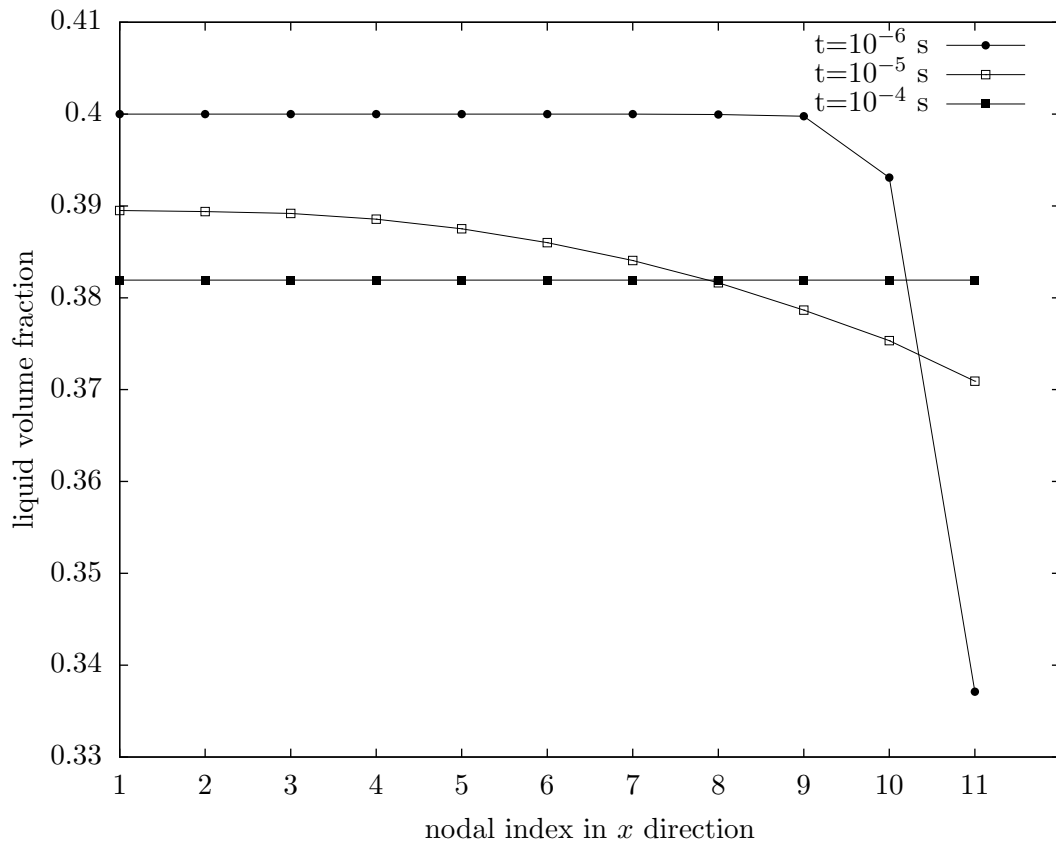


Figure 4: Stretching of a saturated cube: Liquid volume fraction at the nodes along the centerline of the stretch direction at different times (nodes are indexed from 1 to 11 with the latter being on the stretched side)

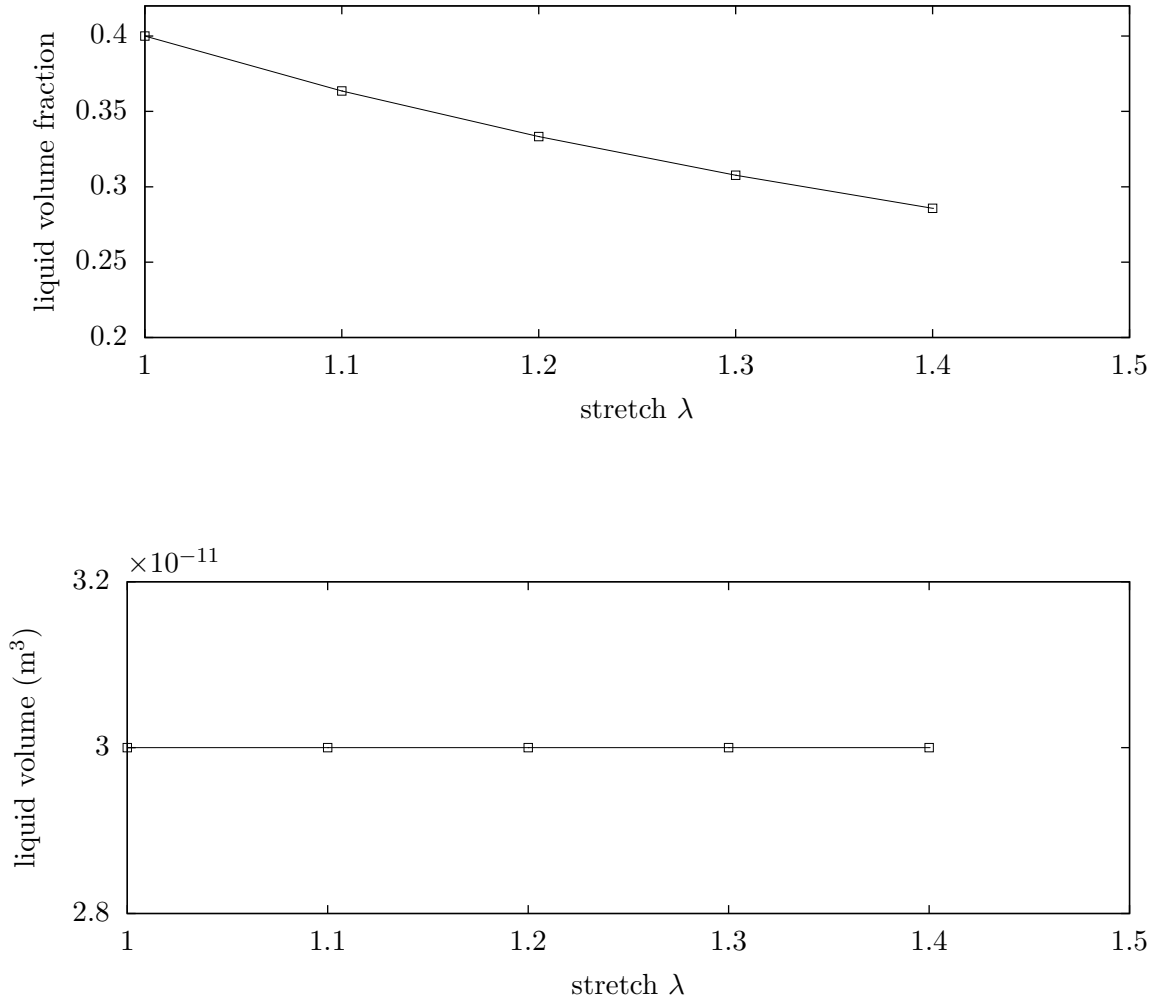


Figure 5: Stretching of a saturated cube: Liquid volume fraction at steady-state as a function of stretch (top) and conservation of liquid volume (bottom)

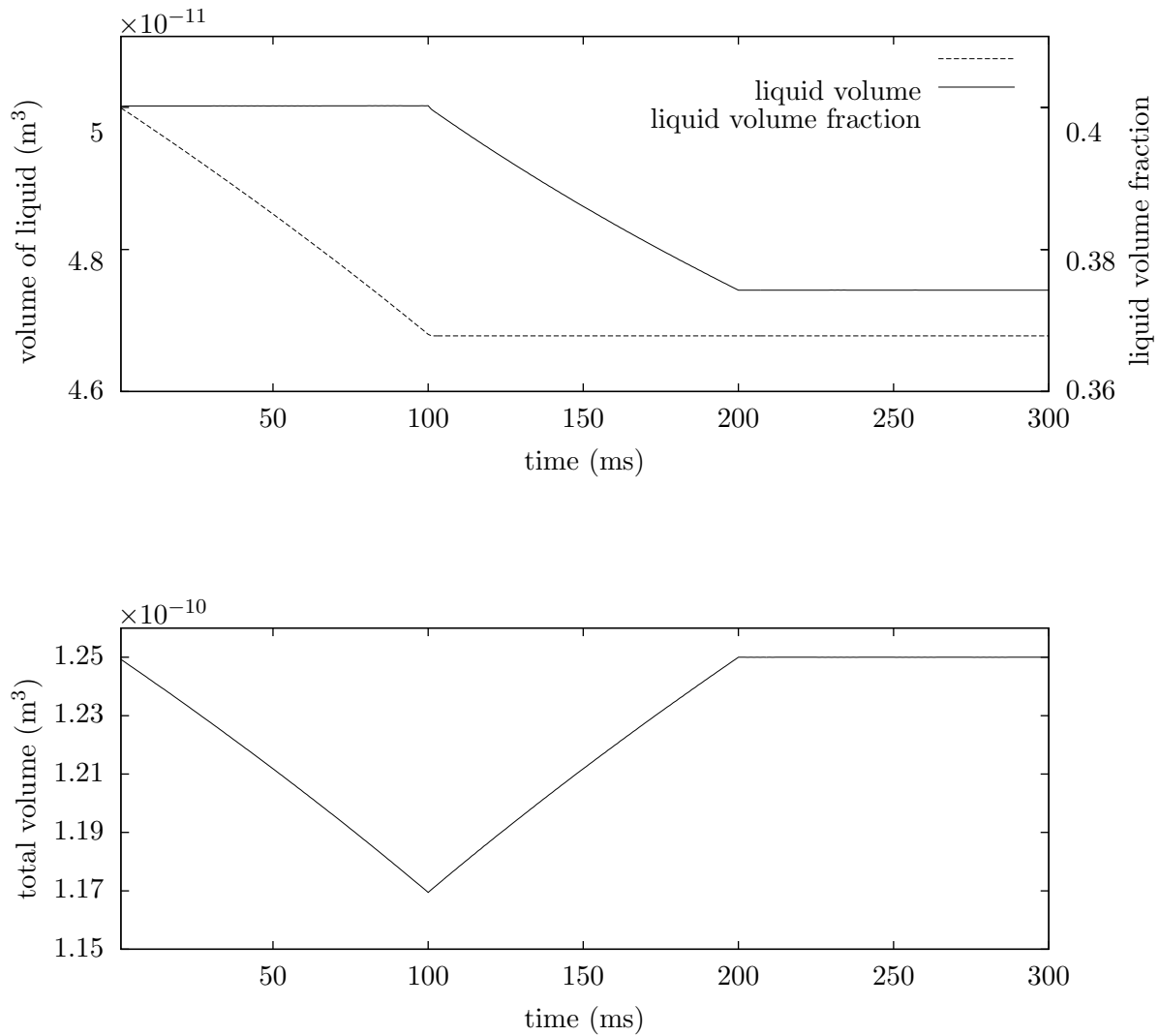


Figure 6: Squeezing of a saturated cube: Liquid and total volume as a function of time

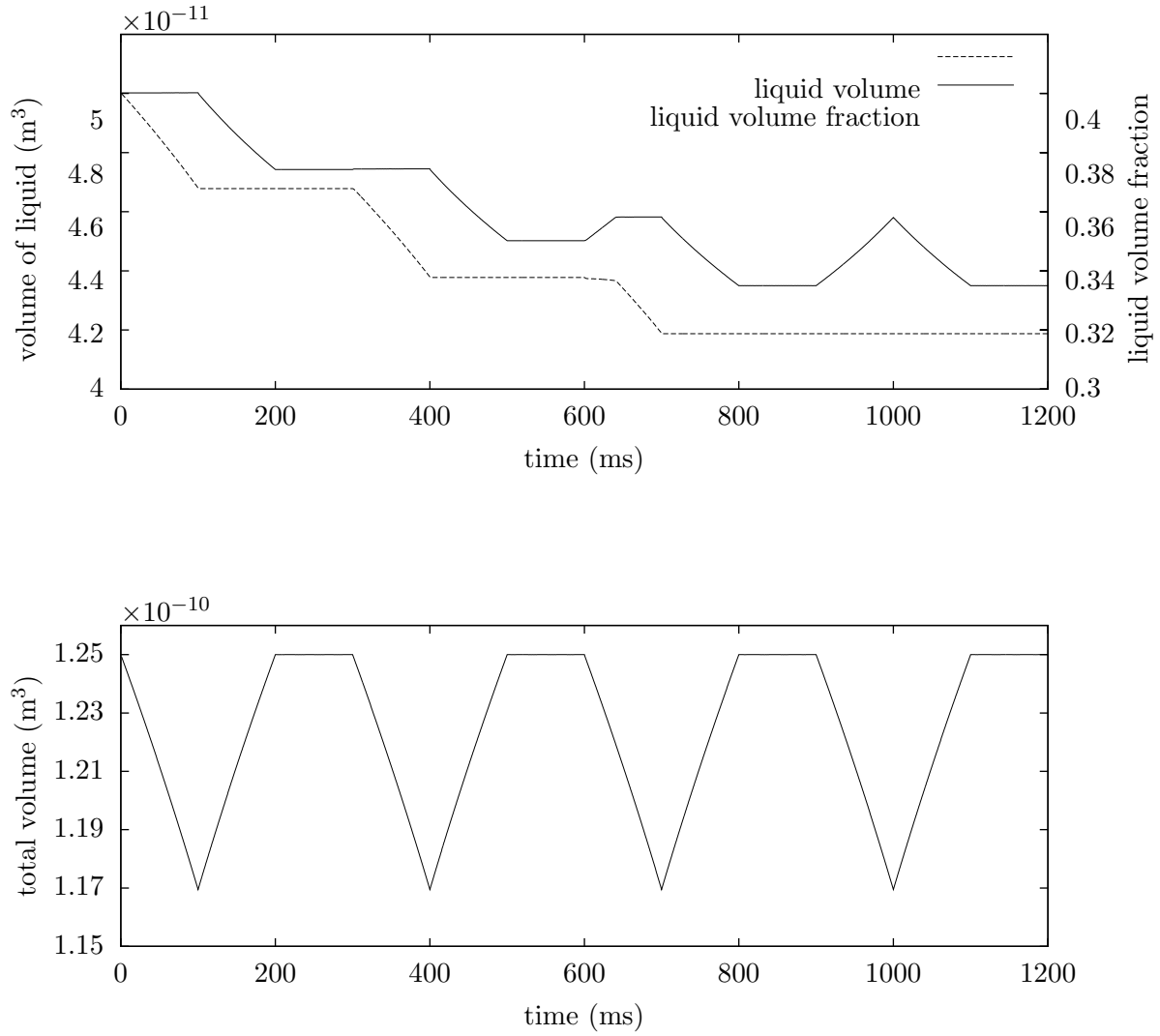


Figure 7: Squeezing of a saturated cube: Liquid and total volume as a function of time for the case of repeated squeezing

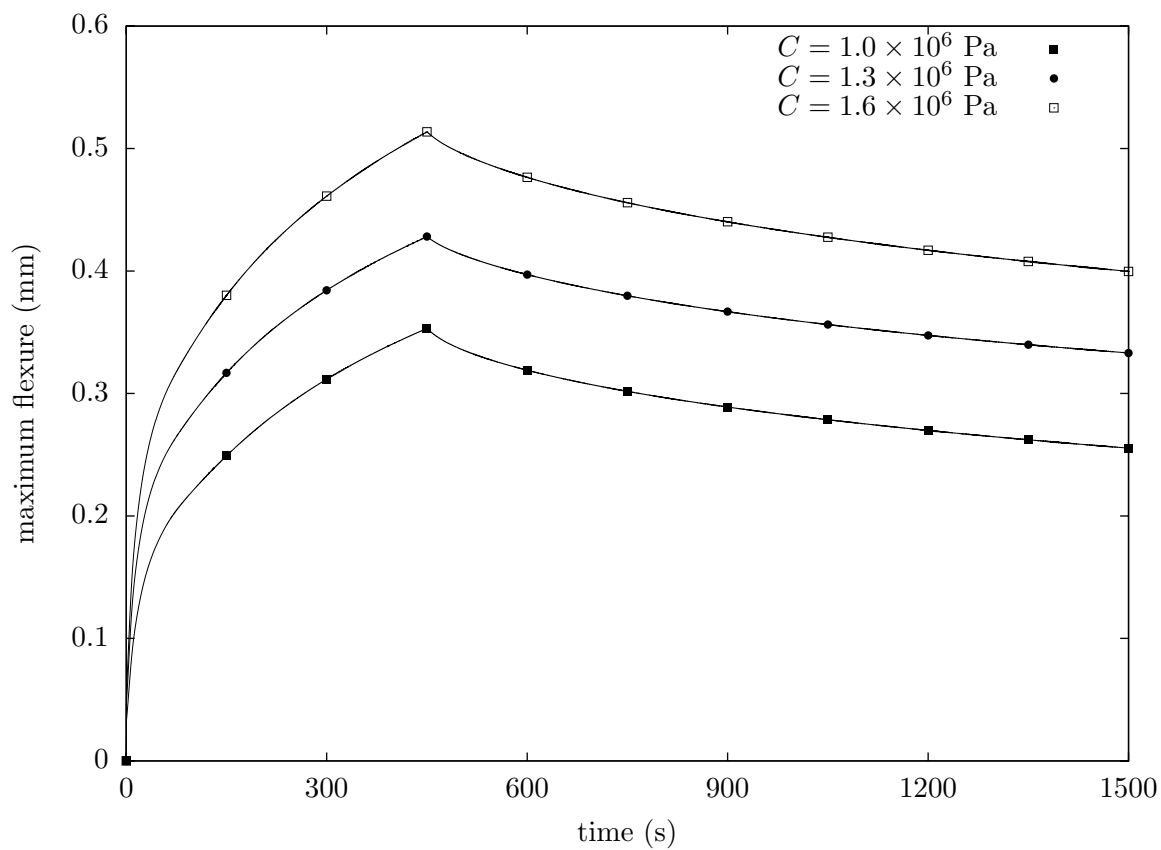


Figure 8: Flexure of a Nafion[®] film due to water absorption: History of maximum flexure for three different values of the liquid pressure constant C

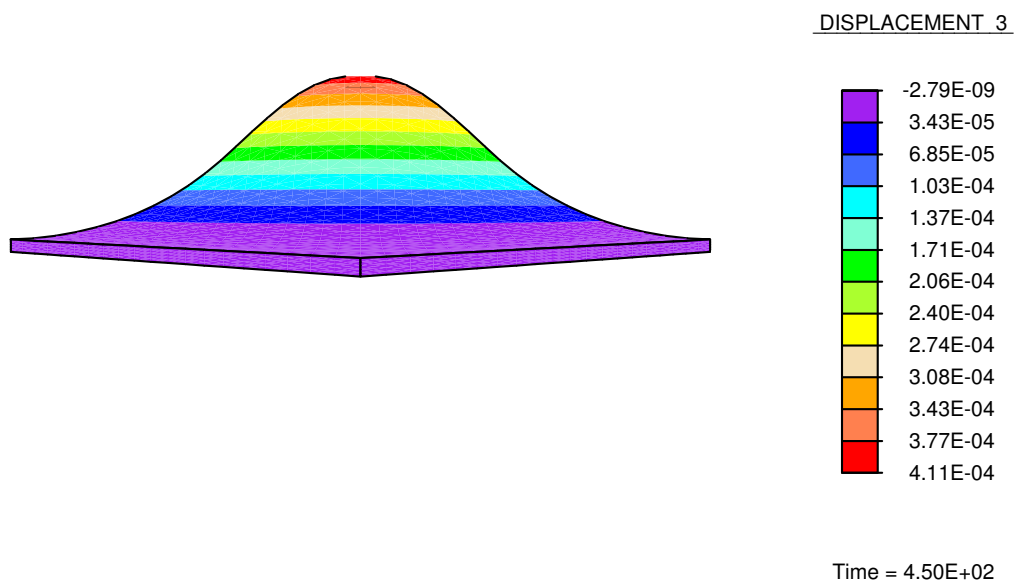


Figure 9: Flexure of a Nafion film, in meters, due to water absorption: Deformed configuration and contour plot of transverse displacement (note that the displacement is scaled by a factor of 5)